ACS OMEGA

http://pubs.acs.org/journal/acsodf

Article

Research on Thermal Behaviors and NO_x Release Properties during Combustion of Sewage Sludge, Sawdust, and Their Blends

Wenjun Yang, Li Zou, Huaishuang Shao, Qinxin Zhao,* and Yungang Wang

Cite This: *ACS Omega* 2022, 7, 20172−20185

Read Online

ACCESS | Metrics & More | Article Recommendations

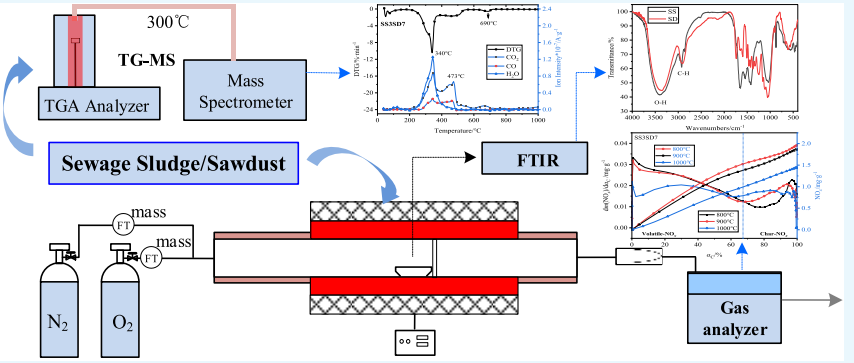

ABSTRACT: To investigate the thermal behaviors and NO_x emission properties during combustion of sewage sludge (SS), sawdust (SD), and their blends (SS5SD5, SS3SD7, and SS1SD9 with SD proportions of 50, 70, and 90 wt %, respectively), tests were conducted using thermogravimetry−mass spectrometry (TG-MS), Fourier transform infrared spectroscopy (FTIR), and a tube furnace in this study. Results indicated that hydrogen in the fuel was mainly released during volatile combustion, and carbon conversion proceeded during the whole combustion process. With the SD proportion increasing, samples exhibited better combustion characteristics. Compared to SD, SS emitted more NO_x due to its higher nitrogen content but showed lower conversion ratios from fuel nitrogen to NO_x, and the NO_x yields decreased significantly with the increase in SD proportion. NO_x emissions of higher volatile samples were more sensitive to temperature, and NO_x yields of SD and SS1SD9 continued to decrease from 800 to 1000 °C, whereas NO_x yields of SS, SS5SD5, and SS3SD7 changed slightly from 800 to 900 °C and decreased significantly from 900 to 1000 °C. Synergistic effects of cocombustion on NO_x emission varied with the blending ratio and temperature. SS5SD5 and SS3SD7 always presented a positive NO_x reduction performance, and SS1SD9 exhibited opposite NO_x reduction effects at different temperatures. Synthetically considering the SS disposal capacity, combustion characteristic, and NO_x yield, an SS proportion of around 30% in blends is more recommended in practical applications.

1. INTRODUCTION

Sewage sludge (SS) is an inevitable byproduct of wastewater treatment. The amount of SS has increased steadily worldwide with the rapid expansion of urban cities and wastewater treatment capacities over the past decades.[1,2] Lots of undesirable substances in SS, such as viruses, bacteria, parasites, and heavy metals, pose a constant threat to the environment and human health.[3,4] The common disposal methods of SS include landfill, agricultural application, composting, and incineration, but the practical application of each method varies all over the world.[5−7] Nonstandard or irregular treatments do much harm to the environment and human health. Incineration is an efficient and convenient method to achieve sludge reduction and reutilization, and the abundant numbers of studies on the combustion of solid fuels provide rich research methods and utilization experiences for sewage sludge combustion.[8−11] Considering the poor fuel properties of SS due to its high ash content and low calorific value, a practical way to achieve efficient utilization of SS is cocombustion with some other high-quality fuels such as most agricultural and forestry wastes, which can also make remarkable contributions to the reduction of CO_2 emission.

Considering the high nitrogen content of most SS, the investigation of both thermal behaviors and NO_x release properties is of great significance for the application of cocombustion. Thermogravimetric analysis (TG) has been

Received: April 1, 2022
Accepted: May 9, 2022
Published: May 27, 2022

Table 1. Proximate and Ultimate Analyses and Lower Heating Values (LHVs)[a]

	proximate analysis (wt %)				ultimate analysis (wt %)					
samples	M_{ad}	A_{ad}	V_{ad}	FC_{ad}	C_{ad}	H_{ad}	O_{ad}	N_{ad}	S_{ad}	LHV (MJ/kg)
SS	7.2	47.1	40.5	5.2	22.9	3.5	14.1	4.2	0.97	9.8
SS5SD5	5.2	24.6	59.6	10.6	34.3	5.1	27.6	2.5	0.64	13.5
SS3SD7	4.4	15.7	67.2	12.7	38.9	5.7	33.0	1.8	0.50	15.0
SS1SD9	3.6	6.8	74.8	14.8	43.4	6.3	38.4	1.1	0.36	16.5
SD	3.2	2.3	78.6	15.9	45.7	6.7	41.1	0.8	0.30	17.2

[a]Notes: ad is air-dried basis; M is moisture; A is ash; V is volatile matter; FC is fixed carbon.

Table 2. Ash Compositions of Samples at 550 °C (wt %)

samples	Ca	K	Na	Mg	Fe	Al	Zn	Si	P	S	C	O
SS	16.21	1.54	1.21	5.11	6.60	5.72	0.72	5.84	3.49	1.89	3.10	48.3
SS5SD5	16.09	2.61	1.20	4.97	6.31	5.47	0.69	5.61	3.39	1.83	3.05	48.5
SS3SD7	15.95	3.90	1.19	4.81	5.97	5.17	0.65	5.34	3.27	1.76	2.99	48.7
SS1SD9	15.44	8.58	1.16	4.22	4.71	4.08	0.53	4.34	2.82	1.50	2.76	49.5
SD	13.72	24.61	1.03	2.23	0.42	0.34	0.11	0.93	1.31	0.63	1.99	52.3

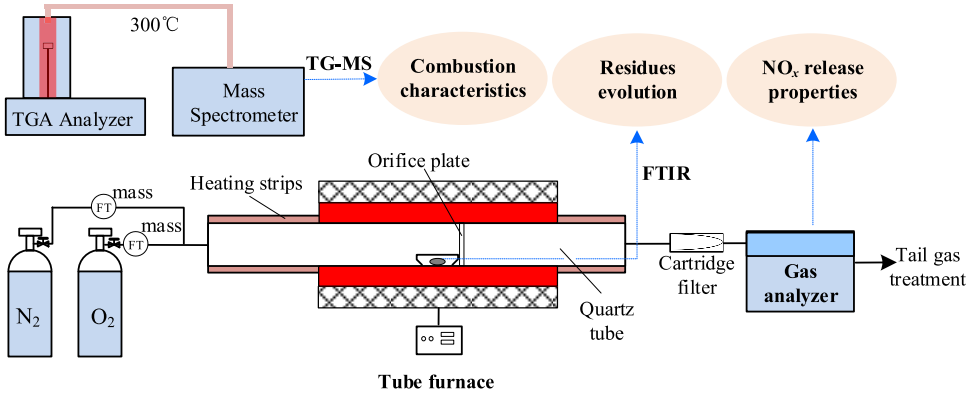

Figure 1. Schematic diagram of the experimental system.

widely used to assess thermal behaviors and kinetics of cocombustion of SS and various fuels. The release of typical gas species during pyrolysis of SS and biomass was also investigated by thermogravimetry−mass spectrometry (TG-MS) and thermogravimetric Fourier transform infrared spectroscopy (TG-FTIR),[12,13] which contributed to the better NO_x emission control. The results of TG-MS analysis during cocombustion of straw and SS suggested an SS proportion of less than 30% in blend fuels.[14] The synergistic effect on NO_x and SO_2 reduction was observed during the cocombustion of SS and three kinds of biomasses.[15] Meanwhile, the study on volatile-N and char-N during pulverized coal combustion in the O_2/CO_2 atmosphere at a high temperature[16] helped obtain the fuel nitrogen conversion mechanism. Previous research on NO_x emission mainly focused on the total yield of NO_x during combustion, whereas the relevance between NO_x release and combustion process has not been discussed in detail. The NO_x release properties versus time make sense, but it is insufficient to assess the NO_x emission during actual combustion due to the uncertainty of burnout time, fuel amount, and airflow velocity. However, the carbon conversion proceeds throughout the entire combustion process and represents the combustion status to a great extent. The carbon conversion ratio always ranges from 0 to 100%, which makes the carbon conversion ratio become an excellent medium for connecting actual combustion with bench-scale tests. Therefore, the NO_x emission versus time and carbon conversion process is indispensable to a better understanding of NO_x emission performance during combustion, which also contributes to more effective and accurate measures for initial NO_x control during combustion.

The mass loss, residue evolution, and NO_x emission properties during combustion were of great importance to the study on combustion of SS and SD and have been discussed in this paper. The mass loss and gas release properties of SS, SD, and their blends in different proportions were investigated by TG-MS analysis under nonisothermal conditions. FTIR analysis was used to investigate the residue evolution characteristics of SS and SD during the heating process in an air atmosphere. Isothermal experiments in a tube furnace were also performed to study NO_x emission properties with the process of time and carbon conversion during combustion. Therefore, a clear understanding of the cocombustion process was obtained, which contributed to evaluating the feasibility of cocombustion of SS and SD, achieving initial NO_x control and eventually finding a practical, secure, and optimized utilization method for these two resources. This study will also provide an important reference for industrial applications of SS and biomass.

2. MATERIALS AND METHODS

2.1. Materials. SS and SD were obtained from a municipal wastewater treatment plant in Yantai (Shandong Province, China) and a poplar wood plant in Hanzhong (Shaanxi

https://doi.org/10.1021/acsomega.2c02015
ACS Omega 2022, 7, 20172−20185

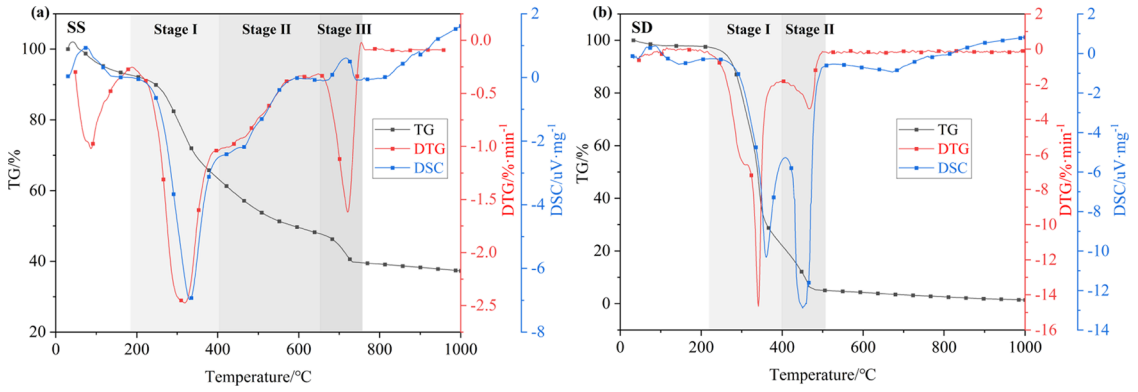

Figure 2. TG, DTG, and DSC curves of (a) SS and (b) SD.

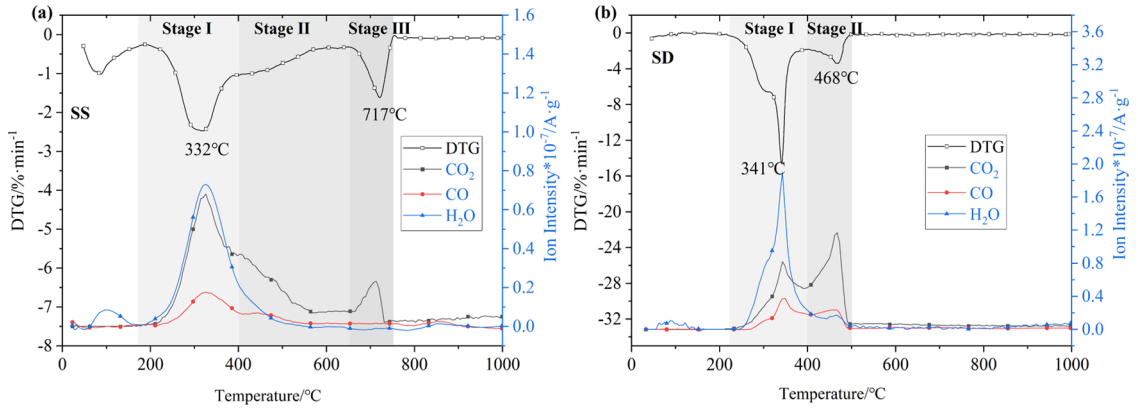

Figure 3. DTG and gas release curves of (a) SS and (b) SD.

Province, China), respectively. Both SS and SD were dried at 105 °C for 24 h in an oven. The dried SS and SD were milled and sieved into 75−147 μm in diameter, and samples for each test were well ground evenly in a mortar by definite mass proportions. Three types of mixtures with SD mass proportions of 50, 70, and 90 wt % were named as SS5SD5, SS3SD7, and SS1SD9, respectively.

The proximate (GB/T 28731-2012) and ultimate (GB/T 28728-2012, GB/T 28732-2012, and GB/T 28734-2012) analysis results and lower heating values (LHVs, GB/T 30727-2014) of samples are presented in Table 1. As shown in Table 1, there were distinct differences between the compositions of SS and SD. With the increase in SD proportion, the average combustible material content increased, the average ash content and nitrogen content decreased, and the fuel properties were remarkably affected. The XRF results of ash at 550 °C are shown in Table 2. SS ash showed remarkable Ca and Fe contents, and the K and Ca were the significant components in SD ash. All three blends presented similar ash compositions to SS due to the much higher ash content of SS than SD.

2.2. Experimental Apparatus and Procedure. In this study, TG-MS tests, FTIR analysis, and tube furnace experiments were conducted, and the schematic diagram of the experimental system is shown in Figure 1.

TG-MS tests of SS, SD, and their blends were conducted by the Thermo Mass Photo instrument. For each test, 5 mg of sample was put into an Al_2O_3 crucible and heated in the TG-MS apparatus at a heating rate of 10 °C/min from room temperature to 1000 °C with a 21 vol % O_2/79 vol % He flow rate of 100 mL/min. The mass loss characteristics were obtained by the TG results, and the release properties of gas products were obtained by the corresponding ion current intensity signals from MS.

To obtain SS and SD residues at specified temperatures, SS and SD were put into a tube furnace (GSL 1200X) with an airflow rate of 1 L/min, and then, the temperature increased from room temperature to preset temperatures (200, 300, 400, 500, 600, 700, 800, and 900 °C) at a heating rate of 10 °C/min. Residues were taken out and cooled with liquid nitrogen immediately when the tube furnace reached the target temperatures. SS, SD, and their residues were analyzed using a Fourier transform infrared spectrometer (Nicolet iS50 FTIR). In addition, to study the NO_x emission properties of SS, SD, and their blends at various combustion temperatures, 0.1 g of samples was put into the tube furnace, which was preheated to 800, 900, and 1000 °C, respectively. Air with a flow rate of 1 L/min was injected into the furnace to provide the necessary oxygen for combustion. A flue gas analyzer (GA-21plus) was used to monitor the O_2, CO_2, CO, NO, and NO_2 concentrations during the whole combustion process. This study was focused on the NO_x yields and the correlation between NO_x release and carbon conversion.

To investigate potential interactions during cocombustion of SS and SD, the experimental and theoretical values for specific parameters, such as TG, NO_x yield, and the ratio of fuel nitrogen to NO_x, were also compared in this study.

3. RESULTS AND DISCUSSION

3.1. Combustion Characteristics of SS and SD. *3.1.1. TG-MS Analysis.* The TG, DTG, and DSC curves of

https://doi.org/10.1021/acsomega.2c02015
ACS Omega 2022, 7, 20172−20185

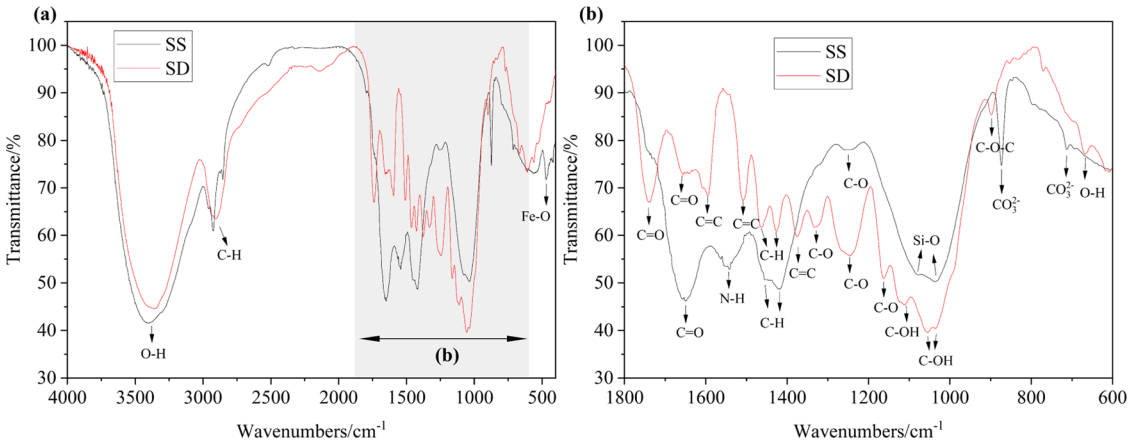

Figure 4. Mid-infrared spectra of (a) SS and (b) SD.

SS and SD at a heating rate of 10 °C/min under a 21 vol % O_2/79 vol % He atmosphere are presented in Figure 2. According to the MS results, strong ion intensity signals of m/z of 18 (H_2O^+), 28 (CO^+), and 44 (CO_2^+) were detected during the heating process. The DTG curves and main gas release curves of SS and SD during the heating process are demonstrated in Figure 3.

As exhibited in Figures 2a and 3a, after a slight weight loss of 7.35% between 40 and 180 °C by the removal of moisture, SS mainly experienced three weight-loss stages during the heating process. A dramatic weight loss of 31.40% between 180 and 400 °C (Stage I) was visible along with the distinct evolution of H_2O, CO_2, and CO corresponding to the devolatilization and combustion of most volatiles. During Stage I, the release of H_2O was mainly related to thermal decomposition reactions (mainly dehydration) and the oxidation of hydrogen in fuel; the CO evolution was mainly caused by the decomposition of labile compositions like alkyl aryl ethers and the oxidization of light hydrocarbyl groups.[17] CO_2 was mainly released from the decomposition of carboxyl and carboxylate groups,[18] as well as the oxidization of carbon-containing compounds. Then, there was a weight loss of 12.81% between 400 and 650 °C (Stage II) with remarkable CO_2 evolution, which mainly resulted from the combustion of residual organics with low reactivity and fixed carbon. Meanwhile, the slight CO yield during Stage II mainly resulted from the incomplete oxidization of carbon. The high ash content of SS decelerated the devolatilization, resulting in a much higher weight loss during Stage II (12.81%) than the fixed carbon content (5.2%) in Table 1. Finally, calcium carbonate decomposition resulted in a weight loss of 9.42% between 650 and 750 °C (Stage III) with abundant CO_2 yield. SS presented a lower final residual mass fraction (m_b) of 38.33% than the ash content of 47.1% (Table 1) mainly due to carbonate decomposition of Stage III.

As shown in Figures 2b and 3b, SD experienced a slight weight loss of 2.33% between 40 and 160 °C with a slight H_2O release peak by the removal of moisture; a sharp weight loss of 74.62% between 220 and 400 °C (Stage I) with remarkable evolution of H_2O, CO_2, and CO corresponding to the devolatilization and combustion of most volatiles; and finally an apparent weight loss of 20.21% between 400 and 500 °C (Stage II), mainly due to the combustion of fixed carbon along with a significant CO_2 yield. The m_b of SD (1.93%) was slightly lower than the corresponding ash content (2.3%) shown in Table 1 due to ash transformation at high temperatures.

The positive and negative values of DSC in Figure 2 represent endothermic and exothermic conditions, respectively. For both SS and SD, the removal of moisture below 180 °C was an endothermic process, and the combustion of volatiles and char corresponded to the distinct exothermic peaks of Stage I and Stage II, respectively. Additionally, the decomposition of $CaCO_3$ during Stage III of SS was an endothermic process. With the temperature further increasing, both SS and SD presented an endothermic process, indicating the existence of mineral transformation in ash. During the whole combustion process, the heat release of SS was 52% less than that of SD, which was consistent with the different calorific values as shown in Table 1. In addition, SS presented a higher heat release ratio of Stage I/Stage II (2.09) than SD (0.90), which mainly resulted from the higher fixed carbon /volatile ratio of SD.

SS and SD presented similar gas evolution properties during Stage I and Stage II. During Stage I, the evolution of H_2O, CO, and CO_2 of SD was mainly caused by the degradation and combustion of hemicellulose, cellulose, and lignin, and the release of H_2O, CO, and CO_2 of SS was mainly due to the decomposition and combustion of lipid, protein, and carbohydrate. SD presented a stronger intensity of H_2O and CO during Stage I than SS due to its higher volatile and hydration contents, suggesting a stronger local reducing atmosphere during devolatilization. During Stage II, the evolution of CO and CO_2 of both SD and SS was mainly due to the combustion of fixed carbon (C-rich materials by aromatic cyclization and graphitization). However, the complex compositions and high ash content in SS resulted in a wider temperature zone of decomposition and higher char combustion temperatures. In addition, for both SS and SD, the conversion of hydrogen to H_2O mainly took place during Stage I, whereas the conversion of carbon to CO_2/CO took place throughout the whole combustion process, which made it reasonable to evaluate the combustion status by the conversion ratio of carbon.

3.1.2. FTIR Analysis. To study the residue evolution properties of SS and SD, FTIR analyses of SS, SD, and their residues at various temperatures were conducted. The mid-infrared spectra of the original SS and SD are shown in Figure 4, and the mid-infrared spectra of residues at multiple temperatures are illustrated in Figure 5. The characteristic

https://doi.org/10.1021/acsomega.2c02015
ACS Omega 2022, 7, 20172−20185

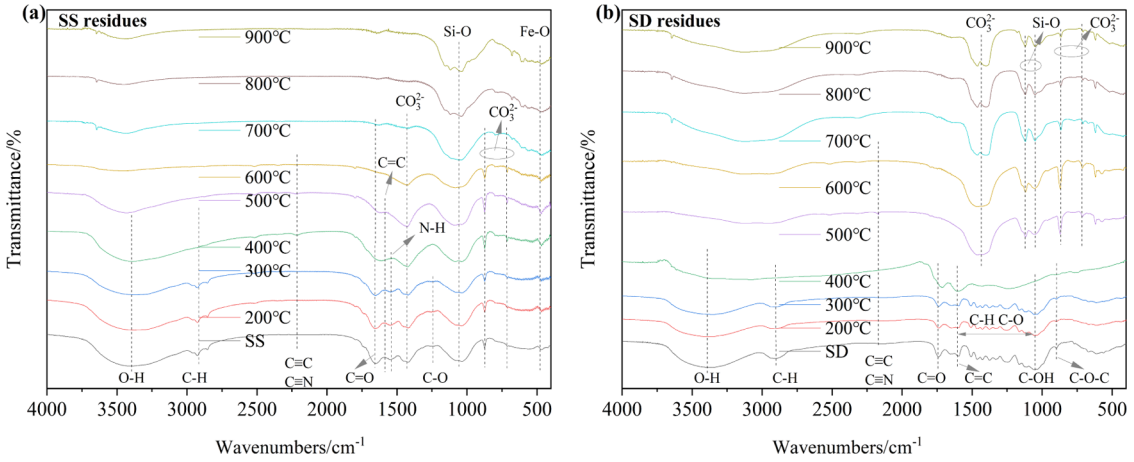

Figure 5. Mid-infrared spectra of (a) SS residues and (b) SD residues.

absorption bands observed in Figures 4 and 5 are presented in Table 3.[19−22]

Table 3. Characteristic Absorption Bands Observed in the Mid-Infrared Spectra

band (cm^{-1})	assignments
3600−3000	O−H stretching of hydroxyl groups or water
3000−2800	C−H stretching of aliphatic methylene or alkyl
2280−2210	C≡C stretching, C≡N stretching
1750−1700	C═O stretching of aldehydes, carboxylates, esters, ketones
1680−1640	C═O stretching of carboxylates (amide I band)
1597, 1509, 1375	C═C stretching of aromatic rings, alkenes
1570−1540	N−H in-plane (amide II band)
1510−1390	CO_3^{2-} stretching of carbonates
1470−1350	C−H deformation of aliphatic compounds
1335−1240	C−O stretching of carboxylates, phenols, ethers
1160	C−O stretching of esters
1100−1000	C−OH stretching of carbohydrates
1080	Si−O stretching of silicates
1058	C−O stretching, glycosidic linkages between sugar units
1035	Si−O stretching of silicates
898	C−O−C stretching of glucose ring (cellulose)
872	CO_{2-3} out-of-plane bending of carbonates
712	CO_3^{2-} in-plane bending of carbonates
668	O−H out-of-plane bending in C−OH alcoholic groups
462	Fe_2O_3

From the SS spectrum presented in Figure 4, there were abundant O−H (3600−3000 cm^{-1}) and C−H (2800−3000 cm^{-1}) bonds in SS, indicating the presence of considerable alcohol and aliphatic compounds. The distinct absorption peak at 1650 cm^{-1} (C═O stretching) corresponded to carboxylates in lipid and protein. The peak at 1543 cm^{-1} corresponded to the overlap of the C═C stretching vibration and the N−H in-plane bending vibration (amides II band). These amide structures mainly originated from abundant DNA and RNA of animal and plant cells and microorganisms in SS. In addition, the high ash content of SS resulted in the distinct band overlap of organic functional groups and inorganic components.[19] The intense peaks at 1456 and 1417 cm^{-1} were mainly owing to the combination of the CO_3^{2-} stretching vibration and the C−H deformation vibration, and the peaks at 1080 and 1035 cm^{-1} corresponded to the combination of the Si−O stretching vibration and the C−O stretching vibration. The SS spectrum indicated the main organic components of lipid, protein, and carbohydrate[22] and the main inorganic components of silica oxides (1080 and 1035 cm^{-1}), carbonates (1456, 1417, 872, and 712 cm^{-1}), and iron oxides (462 cm^{-1}).

From Figure 5a, SS mainly experienced organic evolution from 200 to 600 °C and inorganic evolution from 600 to 800 °C. The desorption of external water mainly occurred below 200 °C. With the temperature increasing from 200 to 400 °C, the quantities of O−H, C−H, and C−O decreased significantly by bond breaking[23] with the release of H_2O, CO_2, and CO, as shown in Figure 3a, and the cleavage of intramolecular H-bonds, the subsequent dehydration, and complex condensation reactions led to the structure rearrangement of carbon (aromatic cyclization and graphitization),[24] which resulted in the stronger absorption of C═C stretching (1597 cm^{-1}) and the absorption of C≡C and C≡N stretchings (2215 cm^{-1}) at 400 °C. When the temperature reached 600 °C, most amounts of C═C (1597 cm^{-1}) and C═O (1650 cm^{-1}) bonds were consumed by oxidation with the release of CO_2, and the residue presented significant features of ash. Then, carbonates (1453, 1417, 872, and 712 cm^{-1}; mainly $CaCO_3$) decomposed between 600 and 800 °C. The relative amounts of carbonates increased with the consumption of organics in SS and then decreased by decomposition.

From the SD spectrum in Figure 4, the intense absorption bands of O−H stretching (3600−3000 cm^{-1}), C−H stretching (2800−3000 cm^{-1}), and C═O stretching (1750−1640 cm^{-1}) were visible, indicating the presence of alcohol, aliphatic compounds, ketones, or short-chain carboxylic acids in SD. Peaks at 1597, 1509, and 1375 cm^{-1} (C═C stretching vibration) corresponded to aromatic rings from lignin compounds. Peaks between 1470 and 1350 cm^{-1} were due to the C−H deformation vibration of cellulose and lignin. Peaks between 1300 and 1100 cm^{-1} resulted from the C−O stretching vibration of carboxylic acids, phenols, or ethers. Peaks between 1100 and 1000 cm^{-1} (C−OH stretching vibration) indicated the presence of carbohydrates like cellulose and hemicellulose. SD was also characterized by the peaks at 1058 and 898 cm^{-1} corresponding to O-glycosidic linkages between sugar units and glucose rings. The FTIR results verified the three main components of hemicellulose, lignin, and cellulose of SD.[25]

From Figure 5b, SD mainly experienced similar residue evolution properties to SS, including the organic evolution

https://doi.org/10.1021/acsomega.2c02015
ACS Omega 2022, 7, 20172−20185

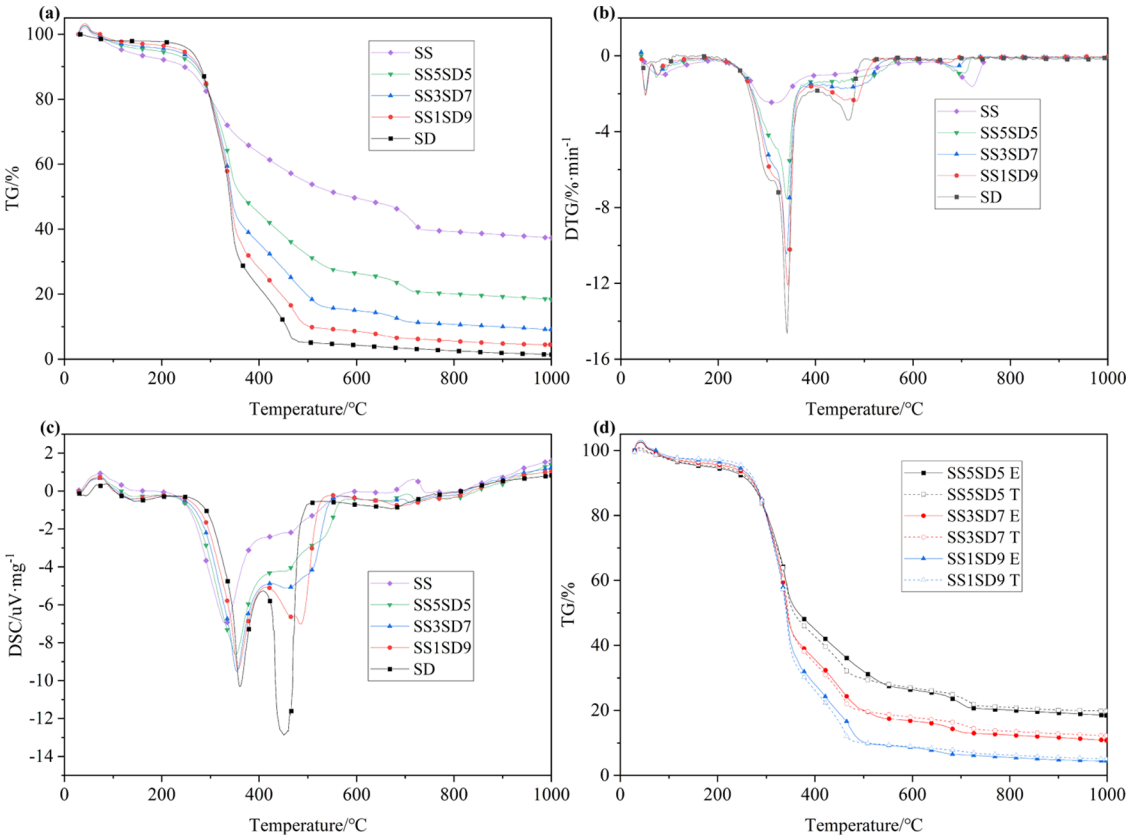

Figure 6. (a) TG, (b) DTG, (c) DSC, and (d) theoretical TG curves of blends (E, experimental value; T, theoretical value).

Table 4. Weight-Loss Stages of SS, SD, and Blends during the Heating Process

	stage I			stage II			stage III	
samples	T (°C)	TG (%)	DSC (%)	T (°C)	TG (%)	DSC (%)	T (°C)	TG (%)
SS	180−400	31.40	67.59	400−650	12.81	32.43	650−750	9.42
SS5SD5	200−400	49.72	57.12	400−620	18.93	42.94	620−750	5.45
SS3SD7	200−400	60.11	53.80	400−600	20.63	46.22	600−750	3.85
SS1SD9	220−400	68.15	50.11	400−600	19.32	49.91	600−750	1.64
SD	220−400	74.62	47.49	400−500	20.21	52.50		

Table 5. Combustion Characteristic Parameters of SS, SD, and Their Blends[a,b,c]

samples	T_i (°C)	T_b (°C)	m_b (%)	T_1 (°C)	DTG_1 (%/min)	T_2 (°C)	DTG_2 (%/min)	T_3 (°C)	DTG_3 (%/min)	DTG_{mean} (%/min)	$S \times 10^{-8}$ ($K^{-3}\cdot min^{-2}$)
SS	246	734	38.33	332	6.55	395	1.07	717	1.63	1.14	2.75
SS5SD5	247	716	21.51	340	15.05	449	1.42	696	0.95	1.55	8.72
SS3SD7	254	701	14.21	340	21.54	457	1.79	690	0.58	1.81	14.44
SS1SD9	262	547	6.15	343	25.06	480	2.39	670	0.35	3.05	32.60
SD	267	505	1.93	341	30.67	468	3.40			3.71	50.15

[a]Notes: T_1, T_2, and T_3 are the temperatures according to DTG peaks of Stage I, Stage II, and Stage III, respectively. [b]DTG_1, DTG_2, DTG_3 are the DTG values at T_1, T_2, and T_3, respectively,. [c]DTG_{mean} is the average mass loss rate during the whole mass loss process.

from 200 to 500 °C and inorganic evolution from 500 to 800 °C. After the removal of external moisture below 200 °C, the amounts of O−H, C−H, and C−O−C of the glucose ring and O-glycosidic linkages between sugar units gradually decreased by decomposition and oxidization;[23] meanwhile, complex condensation and rearrangement reactions took place below 400 °C with the generation of C-rich compounds and the release of H_2O and CO_2, as shown in Figure 3b, resulting in the stronger C═C vibration (1597 cm^{-1}) and C≡C vibration (2215 cm^{-1}) at 400 °C. Compared to SS, SD exhibited a lower burnout temperature of about 500 °C, during which C═C (1597 cm^{-1}) and C═O (1737 cm^{-1}) got nearly exhausted, and strong inorganic peaks (Si−O stretching at 1088 and 1035 cm^{-1}, CO_3^{2-} vibration at 1450 and 872 cm^{-1}) became visible. The carbonates (mainly $CaCO_3$ and K_2CO_3) gradually decomposed with the further increase in temperature from 600 to 800 °C.

3.2. Combustion Characteristics of Blends. The TG, DTG, and DSC curves of all samples as well as the experimental and theoretical TG curves of blends are shown

https://doi.org/10.1021/acsomega.2c02015
ACS Omega 2022, 7, 20172−20185

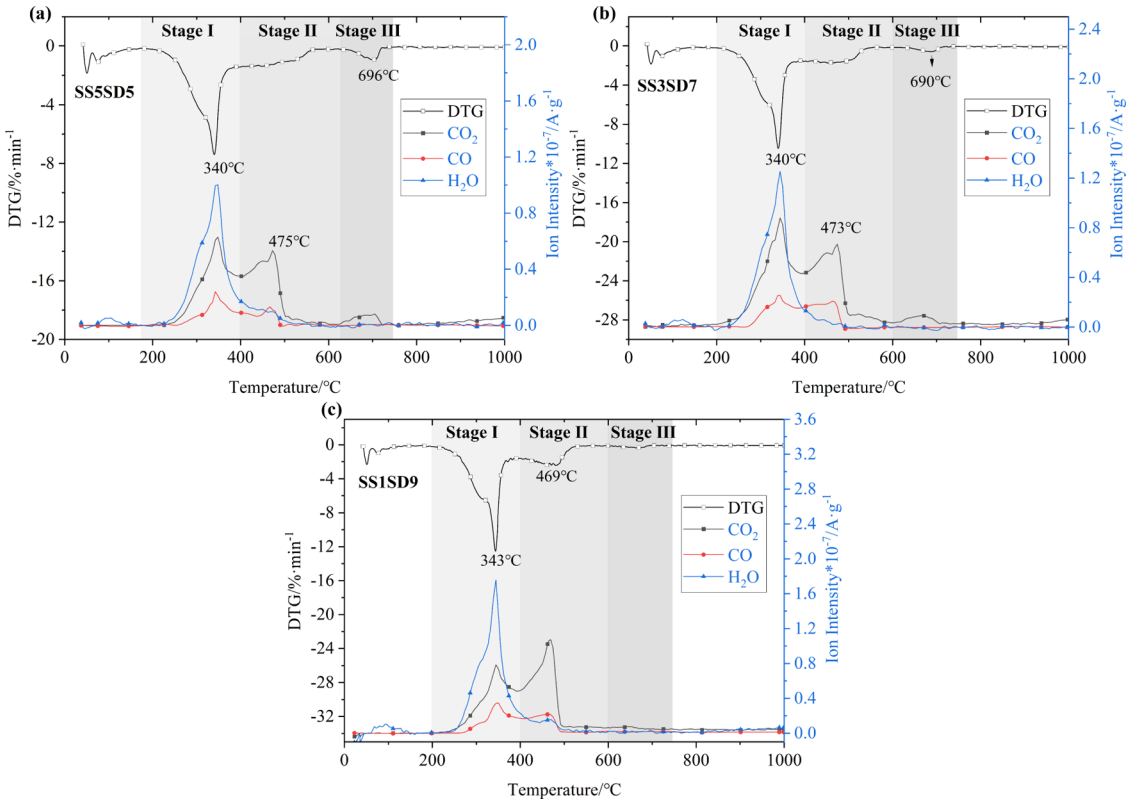

Figure 7. DTG curves and gas release curves of (a) SS5SD5, (b) SS3SD7, and (c) SS1SD9.

in Figure 6. The TG, DTG, and DSC curves of blends exhibited a significant correlation with the blending ratio.

Blends presented three main weight-loss stages during the heating process: Stage I (devolatilization and combustion of most volatiles), Stage II (combustion of fixed carbon and residual volatiles), and Stage III (decomposition of carbonates), and the details are shown in Table 4. Blends presented higher initial temperatures of Stage I and lower final temperatures of Stage II than SS due to the addition of SD. With the SD proportion increasing, the weight loss of Stage I increased significantly, whereas the heat release ratio of Stage I/Stage II decreased, which was mainly due to the remarkable increase in the calorie-rich fixed carbon. Meanwhile, blends with higher SD proportions presented lower weight-loss ratios of Stage III due to the lower carbonate contents, and the increased heat release during combustion resulted in the earlier decomposition of carbonates during Stage III.

The combustion parameters were also calculated by the TG-DTG curves and are presented in Table 5. T_{max} is the temperature with the maximum mass loss rate; the ignition temperature (T_i) is defined as the intersection of the tangent at T_{max} and the horizontal curve at the temperature starting to lose weight concerning the TG curve; and the burnout temperature (T_b) is the temperature where the mass loss of samples reached 98% of the total mass loss. The combustibility index S is used as a criterion for fuel combustion characteristics. A bigger S indicates a better combustion characteristic, and S is defined as follows[26]

$$S = \frac{DTG_{max} DTG_{mean}}{T_i^2 T_b} \quad (1)$$

where DTG_{max} denotes the maximum mass loss rate (%/min), DTG_{mean} is the average mass loss rate (%/min), T_i is the ignition temperature (K), and T_b is the burnout temperature (K).

As shown in Table 5, SS exhibited a lower T_i but much higher T_b and m_b than SD, and the DTG_1 and DTG_{mean} of SS were much smaller than those of SD due to their different components. The index S of SS (2.75×10^{-8} $K^{-3}\cdot min^{-2}$) was much smaller than that of SD (5.015×10^{-7} $K^{-3}\cdot min^{-2}$), which indicated that SD had better combustion characteristics than SS.

With the increase in SD proportion, m_b of blends decreased proportionally, and both DTG_1 and DTG_{mean} increased due to the increasing volatile content and combustible material content. Meanwhile, T_i increased slightly and T_b decreased significantly due to the higher T_i and lower T_b of SD. The increasing S indicated that blends with higher SD proportions exhibited better combustion properties.

In addition, the comparison of experimental and theoretical TG curves of blends is shown in Figure 6d. The theoretical values are calculated as follows

$$TG_T = p_{SD} \cdot TG_{SD} + p_{SS} \cdot TG_{SS} \quad (2)$$

where TG_{SD} and TG_{SS} are the experimental TG values of SD and SS, respectively, and p_{SD} and p_{SS} are the mass proportions of SD and SS in blends, respectively.

The experimental TG curves before 340 °C were in good agreement with theoretical curves, which suggested that the decomposition of labile compounds was barely influenced by cocombustion. Nonetheless, the experimental weight-loss ratios were smaller than the theoretical values between 350 and 500 °C for all blends, especially for SS5SD5. During cocombustion, SS ash slowed down the devolatilization and char combustion of SD by decelerating heat transfer and oxygen diffusion, and therefore, more time or a higher

https://doi.org/10.1021/acsomega.2c02015
ACS Omega 2022, 7, 20172−20185

temperature was required for the combustion process, which was undesirable in practical applications. In addition, blends presented higher burnout ratios than theoretically, and the experimental m_b values of SS5SD5, SS3SD7, and SS1SD9 were higher than the calculated values by 1.23, 1.38, and 0.56%, respectively. During cocombustion, volatiles in SD were released rapidly to generate loose structures with abundant pores in char, which promoted the oxygen diffusion in SS char and contributed to the higher burnout ratios of blends. In addition, the higher calorific value of SD increased the interior temperature of residues, which also promoted burnout and ash decomposition. On the whole, cocombustion of SS and SD showed positive effects on improving fuel properties, and SS3SD7 exhibited optimum interactions during combustion.

The gas release curves of blends during the heating process are demonstrated in Figure 7. Three blends presented similar evolution properties of H_2O, CO, and CO_2 to individual SS and SD. Most H_2O was released during Stage I, while CO and CO_2 presented considerable release yields during both Stage I and Stage II, which suggested that the conversion of hydrogen of blends mainly took place during Stage I and the conversion of carbon took place throughout the whole combustion process. In addition, the intensity of both H_2O and CO_2 got stronger with the SS proportion increasing.

The carbon in the fuel was continuously converted to flue gas during the whole combustion process, and the carbon conversation ratios of SS, SD, and blends during different weight-loss stages are calculated as follows and illustrated in Table 6

$$\alpha_{Ci} = m_{Ci}/m_C \cdot 100\% \quad i = 1,\ 2,\ 3 \tag{3}$$

Table 6. Carbon Conversion Ratios of Samples during Different Weight-Loss Stages

samples	SS	SS5SD5	SS3SD7	SS1SD9	SD
α_{C1}/%	55.9	50.7	49.2	48.3	46.9
α_{C2}/%	34.4	43.7	48.7	51.1	53.1
α_{C3}/%	9.7	4.3	2.1	0.6	
$\alpha_{C2}/(\alpha_{C1}+\alpha_{C2})$	0.381	0.457	0.497	0.514	0.531
FC_{ad}/C_{ad}	0.227	0.309	0.326	0.341	0.348

where α_{C1}, α_{C2}, and α_{C3} denote the carbon conversion ratio during Stages I, II, and III, respectively; m_{C1}, m_{C2}, and m_{C3} denote the relative carbon amounts in both CO and CO_2 released during Stages I, II, and III, respectively; and m_C denotes the total relative carbon amount in both CO and CO_2 released during the whole heating process. The relative carbon amount in CO and CO_2 is obtained by the line integral of CO and CO_2 release curves versus temperature.

With the increase in SD proportion, α_{C1} and α_{C2} gradually increased, which was mainly due to the increasing volatile contents and fixed carbon contents in samples. The $\alpha_{C2}/(\alpha_{C1}+\alpha_{C2})$ ratios were higher than the FC_{ad}/C_{ad} ratios for all samples, which demonstrated that there was a distinct overlap between the combustion of volatiles and fixed carbon. In addition, samples with higher SD proportions presented a much lower α_{C3} due to the much lower carbonates in blends.

3.3. NO_x Emission Properties. The NO_x emission during combustion mainly resulted from three sources: fuel NO_x, thermal NO_x, and prompt NO_x,[27] but the thermal NO_x and prompt NO_x were mainly generated above 1500 °C. Therefore, the NO_x in this study was considered as fuel NO_x, which came from nitrogen in the fuel. A flue gas analyzer was used to monitor the concentrations of O_2, CO_2, CO, NO, and NO_2 during the isothermal combustion in a tube furnace, and NO_x concentration ($c(NO_x)$) was considered as the total concentration of NO and NO_2. According to the monitoring results, the CO concentration was maintained below 50 mg/m^3 during the whole combustion process, indicating the complete combustion of samples.

During volatile combustion, fuel nitrogen was partly transformed to NO_x or N_2 by complex oxidation−reduction reactions and generated heterocyclic-N, amine-N, and nitrile-N compounds,[28] which were further released during char combustion. The NO_x could be roughly divided into volatile-NO_x released during the combustion of volatile and char-NO_x released during char combustion.[16] To obtain the correlation between NO_x release and the combustion process, the conversation ratio of carbon in fuel to CO_2 (α_C) was studied, and α_C as a function of time t is calculated as follows

$$\alpha_C = m_t(CO_2)/m_0(CO_2) \times 100\% \tag{4}$$

where $m_t(CO_2)$ denotes the amount of CO_2 released before time t, and $m_0(CO_2)$ denotes the total amount of CO_2 released during the whole combustion process. The amount of CO_2 is obtained by the line integral of CO_2 release curves versus time.

3.3.1. NO_x Emission Properties of SS and SD. The $c(NO_x)$ and α_C as a function of time during the combustion of SS and SD at 800, 900, and 1000 °C are demonstrated in Figure 8. With the process of time, the carbon conversion proceeded accompanied by the successive release of volatile-NO_x and

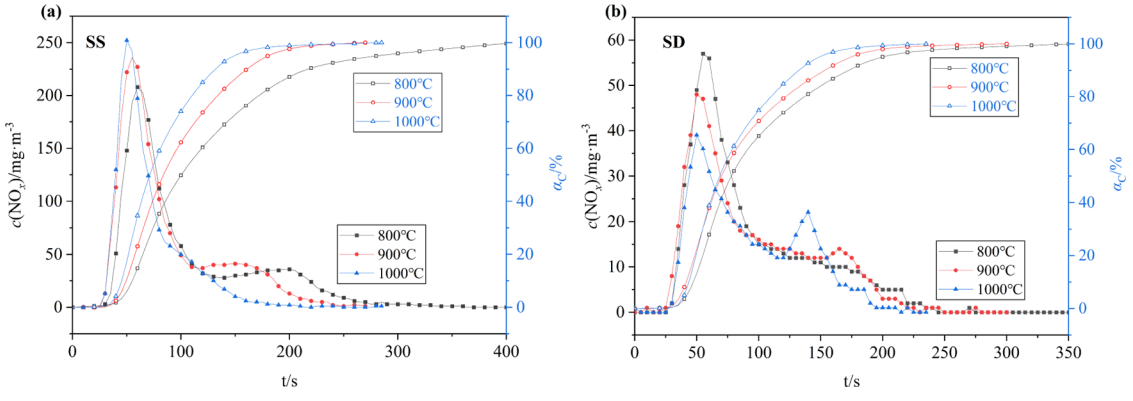

Figure 8. NO_x release curves and α_C-change curves during combustion of (a) SS and (b) SD.

https://doi.org/10.1021/acsomega.2c02015
ACS Omega 2022, 7, 20172−20185

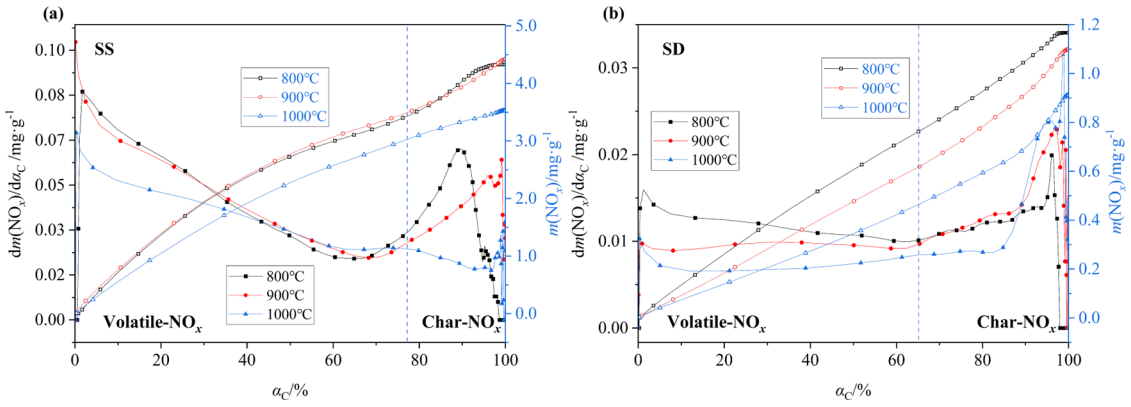

Figure 9. NO_x yield versus α_C during combustion of (a) SS and (b) SD.

char-NO_x. With the temperature increasing, the carbon conversion of both SS and SD was accelerated, and the acceleration effect on SS was stronger than that on SD. SS always presented a much higher volatile-NO_x peak value than SD at different temperatures due to its high nitrogen content, and both SS and SD presented a much stronger volatile-NO_x release peak and a less distinct char-NO_x release peak, indicating the much higher amounts of volatile-NO_x than char-NO_x. With the temperature increasing from 800 to 1000 °C, the enhanced devolatilization contributed to an earlier volatile-NO_x peak with a higher peak value, and the release of char-NO_x also took place much earlier due to the acceleration of char combustion. The boundary between volatile-NO_x and char-NO_x became weak due to the stronger overlap of devolatilization and char combustion at higher temperatures.

To investigate the specific correlation between NO_x emission and the combustion process, the absolute NO_x yield per gram of sample ($m(NO_x)$, mg/g) as a function of α_C and its derivative with respect to α_C ($dm(NO_x)/d\alpha_C$, mg/g, representing the NO_x release amount per unit carbon conversion) are illustrated in Figure 9. Particularly, the total carbon could be divided into volatile carbon and fixed carbon according to Table 1, which contributed to the definition of an imaginary boundary (the dotted lines in Figure 9) between volatile-NO_x and char-NO_x.

As shown in Figure 9a, the $dm(NO_x)/d\alpha_C$ of SS presented a declining trend during volatile combustion (the α_C range of 0−70%) for all temperatures, indicating that more volatile nitrogen released during the earlier carbon conversion stage, whereas the $dm(NO_x)/d\alpha_C$ of SD in Figure 9b changed slightly during volatile combustion (the α_C range of 0−65%) for all temperatures, indicating that the volatile-NO_x of SD was released more uniformly. The nitrogen-containing materials in SS became more independent during the wastewater treatment process and were more likely to decompose with the temperature rising, while nitrogen in SD was mainly uniformly distributed in certain forms and tended to release accompanied by the consumption of volatiles.

The volatile-NO_x release properties varied with temperature. SS presented similar volatile-NO_x yields at 800 and 900 °C but exhibited dramatically lower volatile-NO_x yields at 1000 °C, whereas the volatile-NO_x yields of SD continued to decrease with the increase in temperature. The increasing temperature enhanced the reducing atmospheres of CO, H_2, and hydrocarbyls by the acceleration of devolatilization, which significantly promoted the conversion from fuel nitrogen to N_2 and contributed to volatile-NO_x reduction. In addition, the high volatile content enhanced the effects of temperature on devolatilization, and therefore, SD presented a wider volatile-NO_x-related temperature range.

Temperature also had impacts on char-NO_x of both SS and SD. There was a significant increase in $dm(NO_x)/d\alpha_C$ during the char combustion of SS at both 800 and 900 °C, whereas the corresponding $dm(NO_x)/d\alpha_C$ at 1000 °C exhibited a declining trend and presented much lower values than that at 800 and 900 °C. SS presented similar and considerable char-NO_x yields at 800 and 900 °C but showed a much lower char-NO_x amount at 1000 °C. The abundant metal oxides in SS such as CaO and Fe_2O_3 as shown in Table 2 had positive effects on the reduction of NO_x precursors by generating FeN_x and CaC_xN_y, and the transformation of fuel nitrogen to N_2 was also enhanced by $Ca_2Fe_2O_5$, especially at higher temperatures.[29,30] High temperature also accelerated the generation of CaO by carbonate decomposition and contributed to NO_x reduction. Meanwhile, SS ash with a high slagging potential[31,32] enhanced the fixing of nitrogen in char with the fusion of eutectic mixtures[15] at 1000 °C. Therefore, combustion at 1000 °C presented much less char-NO_x yield.

Nonetheless, temperature had different impacts on char-NO_x of SD. The corresponding $dm(NO_x)/d\alpha_C$ of char-NO_x increased moderately during the whole char combustion process at 800 °C but rose sharply during the last char combustion stage after moderate increases at 900 and 1000 °C. The char-NO_x during the last 10% carbon conversion process increased remarkably with the temperature increasing, and SD presented higher char-NO_x yields at 900 and 1000 °C than at 800 °C. The increasing temperature enhanced the condensation process of combustible materials in SD and probably promoted the transfer of fuel nitrogen into char, which increased the char-NO_x release of SD.

The total NO_x yield and the conversion ratio of fuel nitrogen to NO_x (α_N) of SS and SD at different temperatures are shown in Figure 10, and α_N is calculated as follows

$$\alpha_N = m_N/m_{N0} \times 100\% \quad (5)$$

where m_N denotes the nitrogen amount in NO_x released during the whole combustion process and m_{N0} denotes the total nitrogen amount in the fuel.

The higher nitrogen content of SS as shown in Table 1 led to the higher NO_x yields of SS to a great extent, and the NO_x yields of SD at 800, 900 and 1000 °C were 27.0, 24.9, and 26.4% of that of SS, respectively. Nonetheless, the α_N values of SS at 800, 900, and 1000 °C were smaller than those of SD by 2.29, 1.72, and 1.70%, respectively. The high ash content of SS

https://doi.org/10.1021/acsomega.2c02015
ACS Omega 2022, 7, 20172−20185

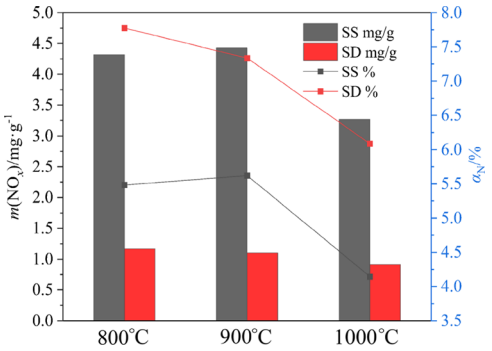

Figure 10. Total NO_x yields and α_N of SS and SD at different temperatures.

slowed down the oxygen diffusion and provided abundant metal oxides with positive nitrogen reduction effects, both of which contributed to the smaller α_N of SS. Furthermore, the ash slagging of SS at high temperatures also fixed more nitrogen in ash. In addition, the total NO_x yield of SD continued to decrease from 800 to 1000 °C, whereas the total NO_x yield of SS experienced a tiny increase from 800 to 900 °C and a remarkable decrease from 900 to 1000 °C, which suggested that the NO_x emission of higher volatile fuels was more sensitive to temperature.

3.3.2. NO_x Emission Properties of Blends. The composition of samples changed with the blending ratio, which had important impacts on NO_x emission properties during combustion. The NO_x release curves versus time, and NO_x yield and $dm(NO_x)/d\alpha_C$ curves versus carbon conversion ratio at 800, 900, and 1000 °C are demonstrated in Figure 11.

The NO_x emission varied remarkably with the blending ratio. As shown in Figure 11, with the SD proportion increasing, the volatile-NO_x concentration reduced significantly, and the total NO_x yield decreased for all temperatures owing to the decreasing nitrogen content. However, the blending ratio exhibited uncertain effects on char-NO_x emission at different temperatures.

Blends with higher SD proportions presented lower $dm(NO_x)/d\alpha_C$ during char combustion and released less char-NO_x at both 800 and 900 °C. The char-NO_x peaks were visible at 800 °C for all blends as shown in Figure 11c, indicating the existence of a concentrated char-NO_x release process, whereas all blends exhibited relatively steady char-NO_x release during the whole char combustion process at 900 °C as shown in Figure 11f. In addition, at 1000 °C, the $dm(NO_x)/d\alpha_C$ during the early and middle stages of char combustion (the α_C range of 60−85%) decreased with the SD proportion increasing, but blends with higher SD proportions presented higher $dm(NO_x)/d\alpha_C$ during the last char combustion process (the α_C range of 90−100%), as shown in Figure 11i, because the char-NO_x of SD tended to release during the last char combustion stage at 1000 °C.

Furthermore, to investigate the effects of temperature on NO_x emission for a specific blend, the NO_x yields and

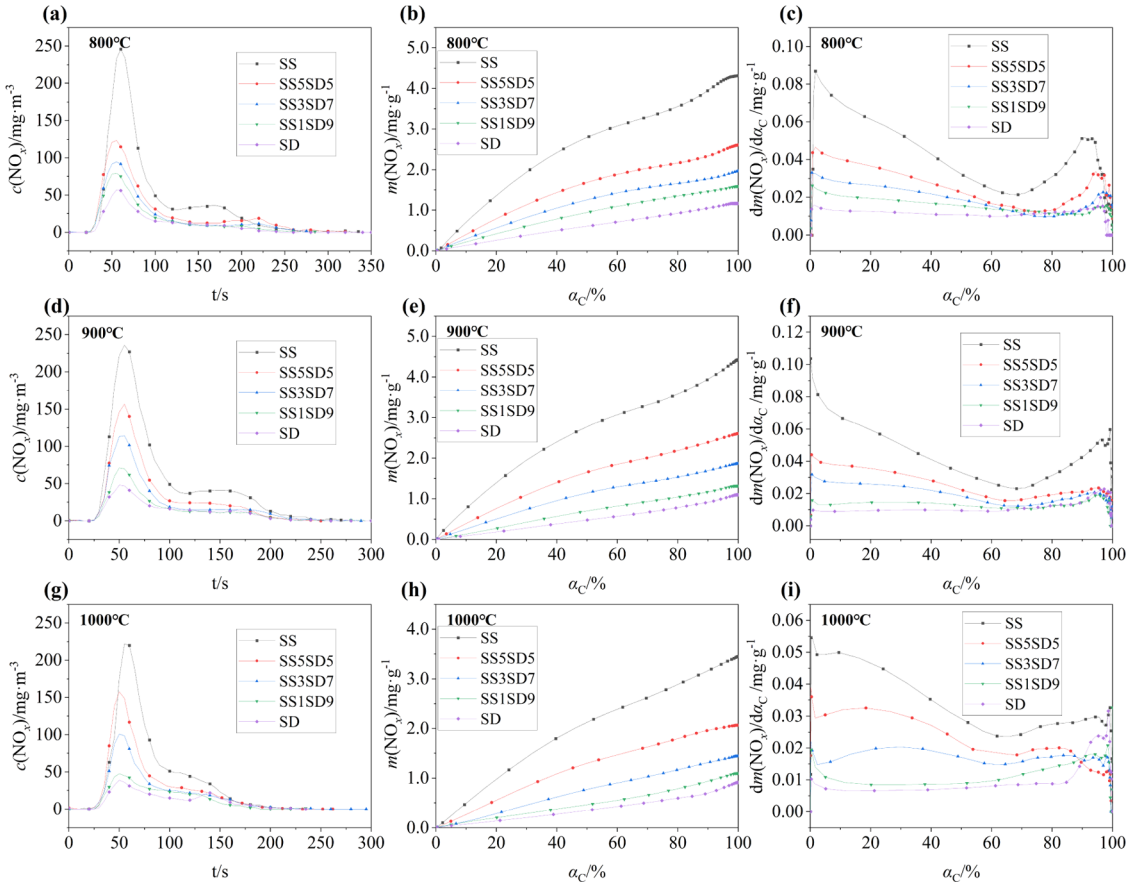

Figure 11. NO_x release curves and NO_x yields versus α_C of blends: (a), (b), and (c) at 800 °C; (d), (e), and (f) at 900 °C; (g), (h), and (i) at 1000 °C.

https://doi.org/10.1021/acsomega.2c02015
ACS Omega 2022, 7, 20172−20185

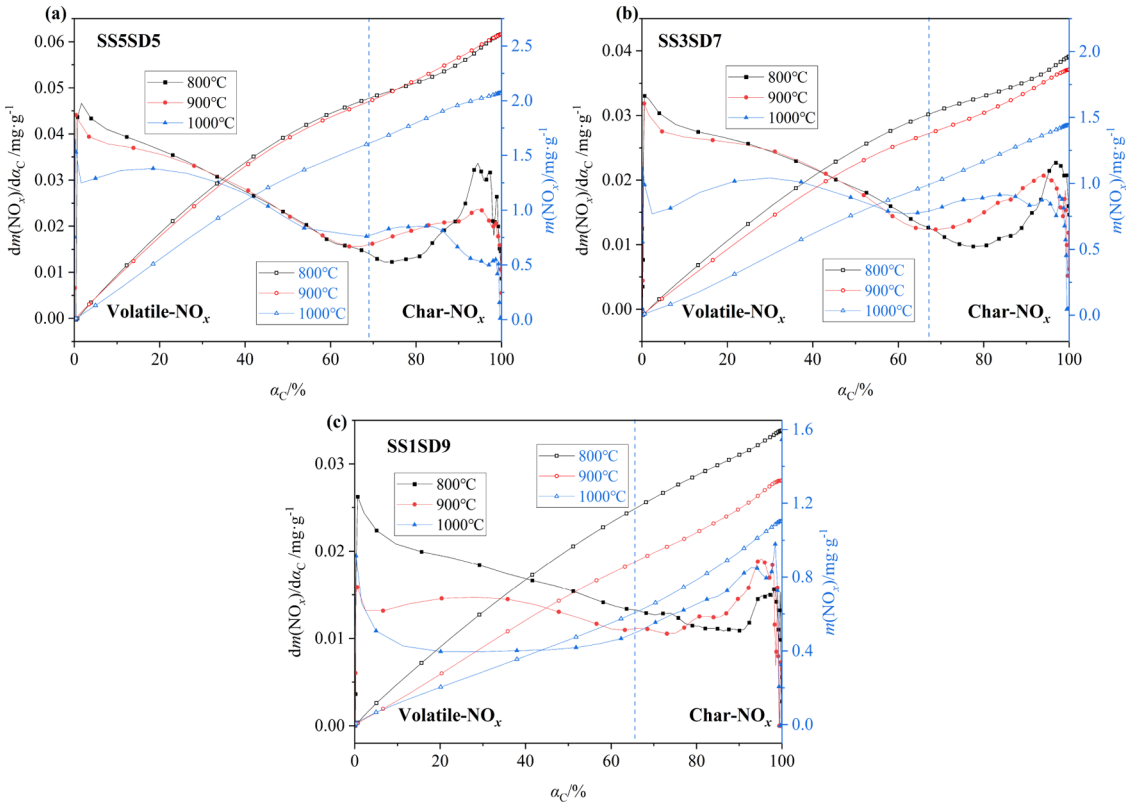

Figure 12. NO$_x$ yield versus α_C during the combustion of (a) SS5SD5, (b) SS3SD7, and (c) SS1SD9.

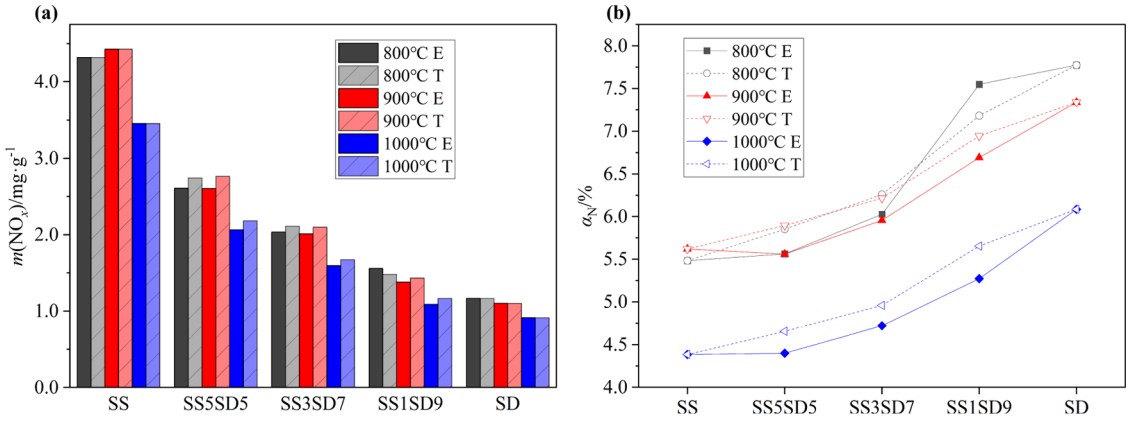

Figure 13. (a) Total NO$_x$ yields and (b) α_N of blends (*E*, experimental value; *T*, theoretical value).

$dm(NO_x)/d\alpha_C$ versus α_C of three blends at different temperatures are illustrated in Figure 12.

Both SS5SD5 and SS3SD7 presented similar volatile-NO$_x$ changing rules with temperature to SS, and SS1SD9 exhibited similar volatile-NO$_x$ changing properties with temperature to SD. The $dm(NO_x)/d\alpha_C$ during volatile combustion of SS5SD5 and SS3SD7 decreased slightly from 800 to 900 °C and then decreased significantly from 900 to 1000 °C. However, the volatile-NO$_x$ of SS1SD9 continued to decrease dramatically from 800 to 1000 °C. The increase in volatile content strengthened the effects of temperature increase on volatile-NO$_x$ release due to the enhanced local reducing atmosphere.

With the increase in temperature, the release of char-NO$_x$ of three blends tended to move toward the earlier carbon conversion process, suggesting that the nitrogen in char was more sensitive to temperature than fixed carbon and the release of char-NO$_x$ proceeded earlier than char combustion. The char-NO$_x$ amount of SS5SD5 changed slightly from 800 to 900 °C and then decreased from 900 to 1000 °C, presenting similar properties to SS. The decrease of char-NO$_x$ from 900 to 1000 °C was mainly due to the severer fusion of eutectic mixtures and the relatively stronger reduction effects of metal oxides in SS at 1000 °C. However, the char-NO$_x$ yields of SS1SD9 continued to increase from 800 to 1000 °C, presenting similar properties to those of SD due to its high SD proportion, and the char-NO$_x$ yield of SS3SD7 increased from 800 to 900 °C and changed slightly from 900 to 1000 °C, which was affected by both SS and SD.

3.3.3. Synergistic Effects on NO$_x$ Emission. To evaluate the synergistic effects of cocombustion, the experimental and theoretical values of the total NO$_x$ yield and α_N of three blends at different temperatures are compared in Figure 13. The

https://doi.org/10.1021/acsomega.2c02015
ACS Omega 2022, 7, 20172−20185

theoretical NO_x yield ($m(NO_x)_T$) during cocombustion is calculated as follows

$$m(NO_x)_T = p_{SD} \cdot m(NO_x)_{SD} + p_{SS} \cdot m(NO_x)_{SS} \quad (6)$$

where $m(NO_x)_{SD}$ and $m(NO_x)_{SS}$ are the experimental values of $m(NO_x)$ for SD and SS, respectively; and p_{SD} and p_{SS} are the mass proportions of SD and SS in blends, respectively. The theoretical α_N is calculated by eq 5 using the theoretical m_N corresponding to $m(NO_x)_T$.

Compared to theoretical values, the NO_x yield of SS5SD5 decreased by 4.9, 5.7, and 5.5% at 800, 900, and 1000 °C, respectively, and the corresponding α_N decreased by 0.29, 0.34, and 0.26% at 800, 900, and 1000 °C, respectively. Cocombustion influenced the local atmosphere during devolatilization and had positive impacts on reducing volatile-NO_x from SS but negative impacts on volatile-NO_x reduction from SD. The NO_x from SS took up the vast majority of the total NO_x of SS5SD5, and therefore SS5SD5 presented an overall volatile-NO_x reduction effect. Meanwhile, compared to individual SS, the more fixed carbon (mainly from SD) strengthened the reducibility of char, and the SS ash in SS5SD5 decelerated the char combustion of SD and lengthened the lifetime of fixed carbon, both of which contributed to the reduction of NO_x from SS. In addition, the abundant metal oxides in SS ash promoted the reduction of NO_x from SD.

The NO_x yield of SS3SD7 decreased by 3.7, 4.2, and 4.8% compared to the theoretical values at 800, 900, and 1000 °C, respectively, and the α_N decreased by 0.23, 0.26, and 0.24% at 800, 900, and 1000 °C, respectively. During the combustion of SS3SD7, the NO_x from SS and SD presented approximate amounts. Compared to individual SS, the higher volatile content of SS3SD7 generated a stronger reducing atmosphere and promoted volatile-NO_x reduction from SS; the fixed carbon from SD and the considerable SS ash also contributed to NO_x reduction; meanwhile, the high SD proportion of SS3SD7 led to a much looser char structure, which enhanced oxygen diffusion and promoted NO_x emission. With the comprehensive effects of various factors, SS3SD7 presented a positive NO_x reduction performance but the synergistic effects were slightly weaker than those of SS5SD5.

Compared to theoretical values, the NO_x yield of SS1SD9 increased by 5.1% at 800 °C and decreased by 3.7% and 6.7% at 900 and 1000 °C, respectively, and α_N presented an increase of 0.36% at 800 °C but decreased by 0.25 and 0.38% at 900 and 1000 °C, respectively. During the combustion of SS1SD9, the NO_x from SD took up the majority of the total NO_x. SS1SD9 presented a much looser structure than SS during combustion, which promoted the oxidation of fuel nitrogen, although SS1SD9 presented a much stronger reducing atmosphere during devolatilization than individual SS. Meanwhile, the small amount of SS ash played little role in NO_x reduction. Therefore, SS1SD9 presented negative NO_x reduction effects at 800 °C. Nonetheless, the effects of reducing atmosphere on volatile-NO_x reduction became enhanced with an increase in temperature, and SS1SD9 showed a positive NO_x reduction performance at 900 and 1000 °C.

In conclusion, the synergistic effects on NO_x emission during cocombustion were complex and influenced by various factors. In this study, the NO_x reduction effects of SS1SD9 were highly dependent on combustion temperature, and SS5SD5 showed better NO_x reduction performances than SS3SD7 at all temperatures. Nonetheless, the NO_x yield of SS5SD5 remained high and the application of SS5SD5 was also severely restricted by the low calorific value and worse combustion characteristics. Synthetically considering the SS disposal capacity, combustion characteristic, and NO_x yield, SS3SD7 is more recommended in practical applications.

4. CONCLUSIONS

The thermal behaviors and NO_x release properties during combustion of SS, SD, and their blends were studied, and the main conclusions are summarized as follows.

(1) All samples experienced dehydration, volatile combustion, char combustion, and ash transformation during the heating process. The conversion of hydrogen to H_2O mainly occurred during volatile combustion, whereas the conversion of carbon to CO_2/CO proceeded during the whole combustion process.

(2) SD exhibited better combustion characteristics than SS, and with the SD proportion increasing, blends exhibited better combustion performances. Compared to theoretical conditions, the burnout ratio increased due to the looser structure of SD, but the combustion of char (mainly from SD) was decelerated by SS ash during cocombustion.

(3) SS emitted more NO_x mainly due to its high nitrogen content than SD but showed a lower α_N owing to its high ash content and high metal oxide content like CaO and Fe_2O_3. Volatile nitrogen in SS existed in less stable forms than that in SD, and the volatile-NO_x release rate versus carbon conversion ratio presented a declining trend for SS but remained relatively stable for SD.

(4) Samples with higher SD proportions released less NO_x due to the lower nitrogen contents. The increase in temperature was more likely to influence the NO_x emission of higher volatile samples. The NO_x yields of SD and SS1SD9 continued to decrease from 800 to 1000 °C, whereas the NO_x yields of SS, SS5SD5, and SS3SD7 changed slightly from 800 to 900 °C and decreased remarkably from 900 to 1000 °C.

(5) Cocombustion exhibited synergistic effects on NO_x emission according to the difference between experimental and theoretical NO_x yields. The blending ratio and temperature affected the synergistic effects by affecting the local atmosphere during devolatilization, oxygen diffusion rate, and the reductivity of char. SS5SD5 and SS3SD7 always presented a positive NO_x reduction performance, and SS1SD9 had opposite NO_x reduction effects at different temperatures. SS5SD5 showed better overall NO_x reduction effects, but its NO_x yields remained high due to its high nitrogen content.

Synthetically considering the SS disposal capacity, combustion characteristic, and NO_x yield, an SS proportion around 30% in blends is more recommended in practical applications, and a study on the correlation between NO_x release and carbon conversion can lay the foundation for efficient initial NO_x control methods during combustion. In addition, due to the differences between bench-scale tests and complicated industrial situations, it is suggested to conduct some relevant actual field tests in the future to obtain a more comprehensive correlation between NO_x release and fuel status.

https://doi.org/10.1021/acsomega.2c02015
ACS Omega 2022, 7, 20172−20185

AUTHOR INFORMATION

Corresponding Author

Qinxin Zhao − *Key Laboratory of Thermal Fluid Science and Engineering of MOE, School of Energy and Power Engineering, Xi'an Jiaotong University, Xi'an 710049, China;* orcid.org/0000-0001-7036-5388; Email: zhaoqx@xjtu.edu.cn

Authors

Wenjun Yang − *Key Laboratory of Thermal Fluid Science and Engineering of MOE, School of Energy and Power Engineering, Xi'an Jiaotong University, Xi'an 710049, China;* orcid.org/0000-0001-9511-1843

Li Zou − *Key Laboratory of Thermal Fluid Science and Engineering of MOE, School of Energy and Power Engineering, Xi'an Jiaotong University, Xi'an 710049, China;* orcid.org/0000-0003-2109-0554

Huaishuang Shao − *Key Laboratory of Thermal Fluid Science and Engineering of MOE, School of Energy and Power Engineering, Xi'an Jiaotong University, Xi'an 710049, China*

Yungang Wang − *Key Laboratory of Thermal Fluid Science and Engineering of MOE, School of Energy and Power Engineering, Xi'an Jiaotong University, Xi'an 710049, China;* orcid.org/0000-0002-2652-9143

Complete contact information is available at: https://pubs.acs.org/10.1021/acsomega.2c02015

Notes

The authors declare no competing financial interest.

ACKNOWLEDGMENTS

This work was supported by the National Key Research and Development Program of China (2021YFC3001803) and the Key Research and Development Program of Shaanxi Province (2018ZDXM-SF-033 and 2017ZDL-G-8-3).

REFERENCES

(1) Yang, G.; Zhang, G.; Wang, H. Current state of sludge production, management, treatment and disposal in China. *Water Res.* **2015**, *78*, 60−73.

(2) Syed-Hassan, S. S. A.; Wang, Y.; Hu, S.; Su, S.; Xiang, J. Thermochemical processing of sewage sludge to energy and fuel: Fundamentals, challenges and considerations. *Renewable Sustainable Energy Rev.* **2017**, *80*, 888−913.

(3) Werther, J.; Ogada, T. Sewage sludge combustion. *Prog. Energy Combust. Sci.* **1999**, *25*, 55−116.

(4) Cieślik, B. M.; Namiesnik, J.; Konieczka, P. Review of sewage sludge management: standards, regulations and analytical methods. *J. Cleaner Prod.* **2015**, *90*, 1−15.

(5) Werle, S.; Wilk, R. K. A review of methods for the thermal utilization of sewage sludge: The Polish perspective. *Renewable Energy* **2010**, *35*, 1914−1919.

(6) Kacprzak, M.; Neczaj, E.; Fijalkowski, K.; Grobelak, A.; Grosser, A.; Worwag, M.; Rorat, A.; Brattebo, H.; Almas, A.; Singh, B. R. Sewage sludge disposal strategies for sustainable development. *Environ. Res.* **2017**, *156*, 39−46.

(7) Kelessidis, A.; Stasinakis, A. S. Comparative study of the methods used for treatment and final disposal of sewage sludge in European countries. *Waste Manage.* **2012**, *32*, 1186−1195.

(8) Bi, H.; Wang, C.; Jiang, X.; Jiang, C.; Bao, L.; Lin, Q. Investigation of sewage sludge and peanut shells co-combustion using thermogravimetric analysis and artificial neural network. *Int. J. Energy Res.* **2021**, *45*, 3852−3869.

(9) Lei, K.; Zhang, R.; Ye, B. Q.; Cao, J.; Liu, D. Study of Sewage Sludge/Coal Co-Combustion by Thermogravimetric Analysis and Single Particle Co-Combustion Method. *Energy Fuels* **2018**, *32*, 6300−6308.

(10) Shi, X.; Zhang, Y.; Chen, X.; Zhang, Y.; Rui, L.; Guo, R.; Zhao, T.; Deng, Y. Numerical simulation on response characteristics of coal ignition under the disturbance of fluctuating heat. *Combust. Flame* **2022**, *237*, 237.

(11) Liu, J.; Huang, L.; Sun, G.; Chen, J.; Zhuang, S.; Chang, K.; Xie, W.; Kuo, J.; He, Y.; Sun, S.; Buyukada, M.; EVRENDILEK, F. (Co-)combustion of additives, water hyacinth and sewage sludge: Thermogravimetric, kinetic, gas and thermodynamic modeling analyses. *Waste Manage.* **2018**, *81*, 211−219.

(12) Wang, S.; Wang, Q.; Hu, Y. M.; Xu, S. N.; He, Z. X.; Ji, H. S. Study on the synergistic co-pyrolysis behaviors of mixed rice husk and two types of seaweed by a combined TG-FTIR technique. *J. Anal. Appl. Pyrolysis* **2015**, *114*, 109−118.

(13) Xu, X. Y.; Zhao, B.; Sun, M. L.; Chen, X.; Zhang, M. C.; Li, H. B.; Xu, S. C. Co-pyrolysis characteristics of municipal sewage sludge and hazelnut shell by TG-DTG-MS and residue analysis. *Waste Manage.* **2017**, *62*, 91−100.

(14) Li, L.; Ren, Q.; Wang, X.; Li, S.; Lu, Q. TG-MS analysis of thermal behavior and gaseous emissions during co-combustion of straw with municipal sewage sludge. *J. Therm. Anal. Calorim.* **2014**, *118*, 449−460.

(15) Wang, Y. G.; Liu, Y.; Yang, W. J.; Zhao, Q. X.; Dai, Y. J. Evaluation of combustion properties and pollutant emission characteristics of blends of sewage sludge and biomass. *Sci. Total Environ.* **2020**, *720*, 137365.

(16) Wu, X. F.; FAN, W. D.; REN, P.; CHEN, J.; LIU, Z.; SHEN, P. H. Interaction between volatile-N and char-N and their contributions to fuel-NO during pulverized coal combustion in O_2/CO_2 atmosphere at high temperature. *Fuel* **2019**, *255*, 115856.

(17) Arenillas, A.; Rubiera, F.; Pis, J. J. Simultaneous thermogravimetric - mass spectrometric study on the pyrolysis behaviour of different rank coals. *J. Anal. Appl. Pyrolysis* **1999**, *50*, 31−46.

(18) Lin, Y.; Liao, Y. F.; Yu, Z. S.; Fang, S. W.; Ma, X. Q. A study on co-pyrolysis of bagasse and sewage sludge using TG-FTIR and Py-GC/MS. *Energy Convers. Manage.* **2017**, *151*, 190−198.

(19) Bekiaris, G.; Bruun, S.; Peltre, C.; Houot, S.; Jensen, L. S. FTIR-PAS: A powerful tool for characterising the chemical composition and predicting the labile C fraction of various organic waste products. *Waste Manage.* **2015**, *39*, 45−56.

(20) Calderón, F.; Haddix, M.; Conant, R.; Magrini-Bair, K.; Paul, E. Diffuse-Reflectance Fourier-Transform Mid-Infrared Spectroscopy as a Method of Characterizing Changes in Soil Organic Matter. *Soil Sci. Soc. Am. J.* **2013**, *77*, 1591−600.

(21) Wu, L. M.; Tong, D. S.; Zhao, L. Z.; Yu, W. H.; Zhou, C. H.; Wang, H. Fourier transform infrared spectroscopy analysis for hydrothermal transformation of microcrystalline cellulose on montmorillonite. *Appl. Clay Sci.* **2014**, *95*, 74−82.

(22) Jimenez, J.; Vedrenne, F.; Denis, C.; Mottet, A.; Deleris, S.; Steyer, J.; Rivero, J. A. C. A statistical comparison of protein and carbohydrate characterisation methodology applied on sewage sludge samples. *Water Res.* **2013**, *47*, 1751−1762.

(23) Zhang, X.; Yang, W.; Blasiak, W. Thermal decomposition mechanism of levoglucosan during cellulose pyrolysis. *J. Anal. Appl. Pyrolysis* **2012**, *96*, 110−119.

(24) GUO, L.; ZHOU, Z.; CHEN, L.; SHAN, S.; WANG, Z. Study of the pyrolysis of coals of different rank using the ReaxFF reactive force field. *J. Mol. Model.* **2019**, *25*, 174.

(25) Yang, H. P.; Yan, R.; Chen, H. P.; Lee, D. H.; Zheng, C. G. Characteristics of hemicellulose, cellulose and lignin pyrolysis. *Fuel* **2007**, *86*, 1781−1788.

(26) Xu, Z. W.; Shao, H. S.; Wang, Y. G.; Zhao, Q. X.; Liang, Z. Y. Characteristics of coal tar residue treated with microwave-assisted hydrothermal treatment. *Fuel Process. Technol.* **2021**, *211*, 211.

(27) Hill, S. C.; Smoot, L. D. Modeling of nitrogen oxides formation and destruction in combustion systems. *Prog. Energy Combust. Sci.* **2000**, *26*, 417−58.

https://doi.org/10.1021/acsomega.2c02015
ACS Omega 2022, 7, 20172−20185

(28) Tian, K.; Liu, W.; Qian, T.; Jiang, H.; Yu, H. Investigation on the Evolution of N-Containing Organic Compounds during Pyrolysis of Sewage Sludge. *Environ. Sci. Technol.* **2014**, *48*, 10888−10896.
(29) Yi, L. L.; Liu, H.; Lu, G.; Zhang, Q.; Wang, J. X.; Hu, H. Y.; Yao, H. Effect of Mixed Fe/Ca Additives on Nitrogen Transformation during Protein and Amino Acid Pyrolysis. *Energy Fuels* **2017**, *31*, 9484−9490.
(30) Tan, H.; Wang, X.; Wang, C.; Xu, T. Characteristics of HCN Removal Using CaO at High Temperatures. *Energy Fuels* **2009**, *23*, 1545−1550.
(31) Donatello, S.; Cheeseman, C. R. Recycling and recovery routes for incinerated sewage sludge ash (ISSA): A review. *Waste Manage.* **2013**, *33*, 2328−2340.
(32) Magdziarz, A.; Wilk, M.; Gajek, M.; Nowak-Wozny, D.; Kopia, A.; Kalemba-Rec, I.; Kozinski, J. A. Properties of ash generated during sewage sludge combustion: A multifaceted analysis. *Energy* **2016**, *113*, 85−94.

https://doi.org/10.1021/acsomega.2c02015
ACS Omega 2022, 7, 20172−20185